

# Supporting Information for “Export of strongly diluted Greenland meltwater from a major glacial fjord”

Nicholas Beaird<sup>1</sup>, Fiammetta Straneo<sup>2</sup>, and William Jenkins<sup>3</sup>

## Introduction

Here we describe the chemical analysis procedure, the water mass analysis used to determine the distribution of glacial meltwater and ocean water masses, and the calculation of the geostrophic velocity used in the export calculations. The chemical and water mass analysis largely follow the methods outlined in *Beaird et al.* [2015] and *Beaird et al.* [2017] but are repeated here with particular values relevant to this study.

## 1. Hydrographic Observations

Temperature, salinity, and pressure data were collected via an internally recording Seabird 25+ CTD at 33 stations in and around Sermilik Fjord. Stations were occupied between 2 - 11 August, 2015. Ship-based CTD data are freely available from the NOAA National Centers for Environmental Information (<http://accession.nodc.noaa.gov/0171277>).

---

Corresponding author: Nicholas Beaird, Department of Physical Oceanography, Woods Hole Oceanographic Institution, Woods Hole, Ma, USA. (nbeaird@whoi.edu)

Noble gas data are freely available at the Biological and Chemical Oceanography Data Management Office (BCO-DMO, <https://www.bco-dmo.org/project/732806>).

## 2. Analytical Methods for Noble Gas Concentration

One hundred water samples (Figs. S1, S2, and S3) were collected using 5 liter Niskin Bottles on a 12 bottle rosette housing a SeaBird 25+ CTD and tripped with an Auto-Fire Module. Observations are shown in temperature-salinity space (Fig. S1), and as depth profiles of concentration (Fig. S2) and saturation anomaly (Fig. S3). Saturation anomaly,  $\Delta_{ng}$ , is the percent difference from saturation equilibrium with air determined using in situ temperature and salinity:

$$\Delta_{ng} = \left( \frac{C_{ng}^{in\ situ}}{C_{ng}^{eq}(\theta, S)} - 1 \right) \times 100 \quad (1)$$

where  $C_{ng}^{in\ situ}$  indicates the in situ concentration of a given noble gas, and  $C_{ng}^{eq}(\theta, S)$  are the solubility equilibrium concentrations. Solubility equilibrium concentrations were determined in a separate set of experiments using the same standardization and the subject of a manuscript in preparation. Preliminary results for these determinations are available at <http://www.whoi.edu/IGF>.

Noble gas samples were acquired from the Niskin bottles using gravity feed through TYGON tubing to fill lengths of 5/8" copper refrigeration tubing (trapping  $\sim 45$  g water in replicate pairs), then each was hydraulically crimp sealed using the method of *Young and Lupton* [1983].

The extracted gases are purified, separated and measured mass spectrometrically using a third generation, WHOI-constructed, statically operated, helium isotope mass spectrometer of branch tube design for fully simultaneous collection of  $^3\text{He}$  and  $^4\text{He}$  with improved

ion optics. It employs a high emission Nier type ion source. The  $^4\text{He}$  branch has a Faraday Cup detector with a low-noise FET-input electrometer and precision high-frequency VFC for digital signal integration. The  $^3\text{He}$  branch uses a Galileo Channeltron operating in pulse counting mode, with high-speed preamplifier and discriminator electronics. The fully automated sample processing line is optimized for processing extracted water samples, and combines a three-stage cryogenics system [Lott, 2001; Lott and Jenkins, 1984; Stanley et al., 2009] with a Pd-catalyst and dual SAES-707 getters for the removal of water vapor, the purification of reactive gases, and the quantitatively reproducible separation of the 5 noble gases (He, Ne, Ar, Kr, and Xe). Helium isotopes ( $^3\text{He}$ ,  $^4\text{He}$ ) are measured using the magnetic sector dual-collecting mass spectrometer to a reproducibility of 0.1%, and the other noble gases using a quadrupole mass spectrometer (QMS) with a triple mass filter and an electron multiplier operated in pulse counting mode. The lighter noble gases (He, Ne, and Ar) are determined using peak-height manometry while the heavier noble gases (Kr and Xe) are measured using a newly developed, modified ratiometric multi-isotope dilution method. The system achieves reproducibility of gas standards of 0.1% for He, Ne, Ar, Kr, and Xe, and approximately 0.15% reproducibility based on the average standard deviation of 11 replicate pairs of water samples. The mass spectrometer gas standards are tied to an atmospheric standard assuming “canonical” atmospheric abundances for the noble gases of 5.24, 18.18, 9340, 1.14, and 0.087 ppm by volume for He, Ne, Ar, Kr, and Xe (Unnumbered table, Section 3.0, page 33 of *COESA* [1976]) to  $\pm 0.05\%$ . Saturation values were computed using solubilities determined assuming the same standardization.

### 3. Optimum Multiparameter Analysis

The goal of our water mass analysis is to determine the distribution of both oceanic waters and Greenland meltwaters in Sermilik fjord. From these distributions we can quantify the glacier-driven water mass transformation, and, along with velocity information, the export of Greenland meltwaters.

To accomplish this goal we use a standard form of water mass analysis called Optimum Multiparameter analysis (OMP) [*Tomczak and Large, 1989*]. The OMP solves an overdetermined set of linear mixing equations which relate each observed parameter (e.g. temperature, salinity, helium) to a combination of endmembers (e.g. Atlantic Water, submarine meltwater, Polar Water) with known or defined properties.

For each of  $m$  measured parameters, a linear mixing equation is written that equates the  $j^{\text{th}}$  observed parameter ( $d_{obs,j}$ ) to the sum of the fractions ( $f_i$ ) of each of the  $n$  defined endmembers multiplied by the value of the  $j^{\text{th}}$  parameter for each endmember ( $A_{ij}$ ):

$$\sum_{i=1}^n f_i A_{ij} = d_{obs,j}. \quad (2)$$

This equation gives the contribution of each pure endmember water mass to the observation at a particular location. We also require that the sum of the fractions must equal one ( $\sum_{i=1}^n f_i = 1$ ). The full system of linear equations is given by:

$$\mathbf{A}\mathbf{f} - \mathbf{d} = \mathbf{r}, \quad (3)$$

where  $\mathbf{A}$  is the  $(m+1) \times n$  matrix of all the endmember values (and the mass conservation equation),  $\mathbf{f}$  is the  $n \times 1$  vector of unknown fractions of endmember water types present in the mixture, and  $\mathbf{d}$  is a  $(m+1) \times 1$  vector of the observed properties at a particular location, and  $\mathbf{r}$  is the  $(m+1) \times 1$  misfit between the observed properties and

the solution. The solution to this system of equations,  $\mathbf{f}$ , is a set of mixing ratios that define the fraction of each endmember water mass present at each observation point. To obtain reliable solutions there must be at least as many constraints (measured properties like temperature, salinity etc) as unknowns (endmember water masses), i.e.  $m + 1 \geq n$ . As shown below, in the case of Sermilik the system is overdetermined by the measured parameters.

The matrix  $\mathbf{A}$  and the observations  $\mathbf{d}$  are standardized and weighted before inversion and minimization [*Glover et al.*, 2011]. Standardization is a process of normalization, required so that the different parameters are comparable. The matrix  $\mathbf{A}$  is standardized by replacing its elements  $A_{ij}$ , with  $\mathcal{A}_{ij} = (A_{ij} - A_j)/\sigma_j$  where  $\sigma_j = \sqrt{(1/n \sum_{i=1}^n (A_{ij} - A_j)^2)}$  and  $A_j = 1/n \sum_{i=1}^n A_{ij}$ . After standardization the parameters in the matrix  $\mathcal{A}$  are nondimensional with zero mean and variation of order 1. The same process is applied to the observation vector  $\mathbf{d}$ . Weights are defined such that each tracer (row of  $\mathbf{A}$ ) has an influence proportional to the ability of that tracer to distinguish the endmember from the others, and inversely proportional to errors in the data or in knowledge of the endmember properties. Weighting and uncertainty are discussed below after the endmembers are defined.

#### 4. Water Mass Endmembers

The OMP water mass analysis requires us to identify a set of endmembers and define their properties for each measured parameter. The sections below give a description of each endmember.

#### 4.1. Subglacial discharge (SGD) Noble Gas Endmember

The endmember values for subglacial discharge are determined by assuming that meltwater formed at the surface of the ice sheet comes into equilibrium with the atmosphere before it enters the englacial hydrological system. We assume that this equilibration happens to meltwater with salinity of 0 and a temperature around 0°C. The WHOI Isotope Geochemistry Facility has redetermined the solubilities of the five noble gases used in this analysis with natural atmospheric abundances over a temperature range from near freezing to 35°C and a salinity range of 0 to 36.7 PSU. The results, believed accurate to about 0.15% are encoded in MATLAB and are available from the authors on request, along with an internal report [*Lott and Jenkins, 2013*] describing the experiment and results. These solubilities are used to define the gas content of the equilibrated 0°C freshwater that becomes subglacial discharge. The values used for the subglacial discharge endmember are given in Table S1.

#### 4.2. Submarine Meltwater (SMW) Noble Gas Endmember

Submarine Meltwater noble gas concentrations derive primarily from the presence of trapped atmospheric gases in the ice matrix which are forced into solution as ice melts under high hydrostatic pressure [*Loose and Jenkins, 2014*]. Noble gas endmembers for the submarine melt component are determined using published values for the mean air content of glacial ice cored from the Greenland Ice Sheet [ $0.113 \pm 0.0085 \text{ cm}^3 \text{ g}^{-1}$ , *Martinerie et al., 1992*]. The gas content of the Submarine Meltwater endmember is adjusted for gravitational separation [*Craig et al., 1988*]. The values used for the submarine meltwater endmember are given in Table S1.

Our analysis cannot distinguish submarine meltwater that derives from icebergs from that which comes directly from the glacier terminus. Both meltwaters have the same air content and create the same gas saturation signals. Thus we have to group iceberg and glacier terminus submarine meltwater into the same category.

#### 4.2.1. Effective temperature of Submarine Melt Water

Submarine meltwater has an effective temperature well below zero, and it is this effective temperature that is used in the OMP [Loose *et al.*, 2009]. This effective temperature takes into account the latent heat required to melt the ice as well as heat required to warm the ice from its temperature to the melting point. The effective temperature of SMW can be written as

$$\theta_{SMW} = \theta_f - \frac{L}{c_p} - \frac{c_i}{c_p}(\theta_f - \theta_i) \quad (4)$$

where  $c_i$  and  $c_p$  are the specific heat capacities of ice and seawater, and  $L$  is the latent heat of fusion [Gade, 1979]. For  $\theta_i = -5^\circ\text{C}$ ,  $\theta_f = -1.5^\circ\text{C}$ ,  $L = 334500 \text{ J Kg}^{-1}$ ,  $C_p = 3980 \text{ J (Kg K)}^{-1}$ , and  $C_i = 2100 \text{ J (Kg K)}^{-1}$ . In the OMP  $\theta_{SMW}$  is  $-87^\circ\text{C}$ , the temperature endmember value for SMW .

#### 4.3. Ancient Ice Melt (AIM)

As reported earlier [Beaird *et al.*, 2015, 2017] West Greenland noble gas samples indicated a departure from atmospheric  $^3\text{He}/^4\text{He}$  and He/Ne ratios. To account for this in the OMP analysis an endmember called Ancient Ice Melt (AIM) was defined based on observations of depressed  $^3\text{He}/^4\text{He}$  ratios and elevated He/Ne ratios. The AIM found in Beaird *et al.* [2015] was determined to have a  $^3\text{He}/^4\text{He}$  ratio of  $0.21 \pm 0.02 R_A$  (where  $R_A$  is the atmospheric ratio) and a He/Ne ratio of  $4.5 \pm 0.5$  times the atmospheric He/Ne

ratio. This enrichment is consistent with the addition of radiogenic helium to the ice bubbles during contact with basement rock, whose isotopic ratio is below  $0.05 R_A$  consistent with theoretical radiogenic helium isotope production ratios [Andrews, 1985; Morrison and Pine, 1955]. Ice core observations [Craig and Scarsi, 1997] show evidence for altered  $^3\text{He}/^4\text{He}$  ratios at the base of the ice sheet.

However, in the current study, the empirically determined  $^3\text{He}/^4\text{He}$  for Sermilik is  $0.83 \pm 0.01 R_A$  combined with a He/Ne ratio of  $1.58 \pm 0.04$  times atmospheric, which implies an added non-atmospheric He component with an isotopic ratio of  $0.54 \pm 0.05 R_A$  (Figure S4). Although substantially higher than theoretical production ratios (*op. cit.*), such high values have been seen in other continental contexts [Castro, 2004; Torgersen *et al.*, 1995], possibly resulting from degassing of relict magmatic emplacements or “leakage” of mantle helium through continental crust. The former supposition is consistent with elevated  $^3\text{He}/^4\text{He}$  ratios (ranging from  $\sim 2$  to  $\sim 20 R_A$ ) that have been observed in olivine phenocrysts in Northeast Greenland [Marty *et al.*, 1998]. Indeed, the greater proximity of the East Greenland (relative to the Beaird *et al.* [2015] West Greenland) site to the Iceland mantle plume and Mid Atlantic Ridge are consistent with this possibility. The anomalous helium isotopic ratio, however significant geologically, does not affect our glacial melt and hydrographic analyses.

In this study we again define an additional glacial endmember, AIM, to account for the departure from atmospheric ratios. We solve the OMP for this endmember separately, but for the purpose of our study of the spreading and flux of meltwater in Sermilik, we group AIM with SMW in the main text.

#### 4.3.1. A note on $^3\text{He}$ from tritium decay

We use  $^3\text{He}$  as a component of the OMP. We therefore note the following about the potential addition of  $^3\text{He}$  from tritium decay. The tritium levels in the glacial melt are very close to, if not identically zero because of the age of the ice. The subsurface ambient ocean end-member waters (AW, PW) have only order 1 TU level tritium. In situ decay of the latter produces only negligible amounts of  $^3\text{He}$  on the timescales associated with the circulation within the fjord, so it has importance only in “setting” the end-member (outside subsurface water)  $\delta^3\text{He}$ . The  $\delta^3\text{He}$  of ambient subsurface waters is only slightly above the solubility equilibrium value (approximately -1.8%), so even that is a minor issue.

#### 4.4. Oceanic water mass endmembers

Three types of ambient ocean waters are present in the Sermilik region (Fig. S5a). These water masses, identified previously [e.g. *Straneo et al.*, 2012], include a warm, salty Atlantic Water (AW), a cold fresh Polar Water (PW), and a thin, near surface, layer impacted by sea ice melt and thermal heating that we call Surface Water (SW) following *Sutherland and Straneo* [2012]. We define temperature, salinity, and noble gas values for each water mass from water samples taken outside and to the east of the fjord. The strong East Greenland Coastal Current flows from northeast to southwest across the mouth of the fjord. Thus stations to the east are upstream with respect to the coastal current, and are likely to contain waters that have not come in contact with the glaciers of Sermilik fjord. We use water samples from a station upstream taken at three depths in the AW,

PW and SW layers (easily identifiable by their temperature-salinity characteristics, Fig. S5a) to define the noble gas concentrations of the oceanic ambients (Table S1, Fig. S5b-g).

## 5. OMP Weights and Uncertainty

### 5.1. Weights

Some measurements are more useful than others in differentiating the endmembers. The usefulness of a particular tracer depends on our uncertainty in the observation, and the range of values exhibited by the various endmembers. The OMP incorporates this fact by assigning a weight to each tracer. We create a weight for each tracer (row of  $\mathbf{A}$ ) that is the ratio of the variance of endmember values ( $\sigma_j^2 = 1/n \sum_{i=1}^n (A_{ij} - A_j)^2$ ) – a measure of tracer  $j$ 's ability to distinguish endmembers – to the largest uncertainty we assign to that tracer ( $\epsilon_{j,max}$ ):

$$W_j = \frac{\sigma_j^2}{\epsilon_{j,max}^2}. \quad (5)$$

Next we need to define  $\epsilon_{max}$  for each tracer.

We do not have a measurement of the characteristics of pure SMW or AIM, so the largest uncertainty for the noble gases comes from assuming a value for the air content of glacial ice. Thus the SMW and AIM noble gas uncertainty is equal to the uncertainty in the air content of glacial ice ( $\pm 8\%$ ) reported by *Martinierie et al.* [1992]. We are also uncertain of the temperature of the glacial ice. Greenland borehole temperatures show a range between  $-10^\circ\text{C}$  and  $0^\circ\text{C}$  [*Lüthi et al.*, 2015]. We take the average ice temperature to be  $-5^\circ\text{C}$  and take the uncertainty to be  $\sim 4^\circ\text{C}$ . This is also  $\epsilon_{max}$  for the temperature equations.

The  $\epsilon_{max}$  for salinity is taken to be 2 PSU from the range of surface salinities observed in the Surface Water outside the fjord, which displays significant variability between casts.

Following *Tomczak and Large* [1989], the weight for the mass conservation constraint is taken to be equal to the weight of the temperature equation, as it has the largest weight. Weights and  $\epsilon_{j,max}$  for each tracer are given in Table S1. The uncertainties assessed for endmember and each measurement are given in Table S2.

An  $(m + 1) \times (m + 1)$  diagonal matrix of weights,  $\mathbf{W}$ , with entries  $W_{jj}$  given by Equation 5 is applied to the system of mixing equations (eqn. 3). The weighted equation is solved by minimizing the norm of the residual ( $\|\mathbf{r}\|^2 = \mathbf{r}^T \mathbf{r}$ ) in a non-negative least squares sense:

$$(\mathbf{A}\mathbf{f} - \mathbf{d})^T \mathbf{W}^T \mathbf{W} (\mathbf{A}\mathbf{f} - \mathbf{d}) = \mathbf{r}^T \mathbf{r}. \quad (6)$$

## 5.2. OMP model fit

The success of the OMP can be evaluated by examining the model-data misfit of the solutions. We substitute the output of the OMP,  $\mathbf{f}$ , into Equation 2 to construct model estimates of the observations. Figure S6 shows the distributions of the difference between the modeled and observed parameters expressed as a percentage, and the r.m.s. misfit is printed for each parameter. A standard metric for acceptable fits is that model-data misfit be less than 5% [*Karstensen and Tomczak*, 1998], a standard that is met for the model used here.

## 5.3. OMP solution uncertainty

Uncertainty in the solutions ( $\mathbf{f}$ ) of the weighted system (Eqn. 6) is tested using a Monte Carlo method. For each of the 100 observations, 5000 perturbed versions of the design matrix,  $\mathbf{A}'$ , are created by replacing all elements  $A_{ij}$  with  $A'_{ij}$ , where  $A'_{ij}$  is a perturbed endmember value selected from a random normal distribution with mean  $A_{ij}$  (Table S1) and standard deviation reflecting the uncertainty in  $A_{ij}$  (i.e.  $\epsilon_{ij}$  from Table S2). We then solve each perturbed system to obtain a set of perturbed solutions  $\mathbf{f}'$ . We take the standard deviation of the perturbed system solutions  $\mathbf{f}'$  to be representative of the systematic error in the water mass fractions due to the OMP method. The resulting solutions and error distributions are shown in Figure S7. We have, as is the case in the main text, combined the AIM and SMW endmembers in the first panel – considering them equivalent submarine meltwater types as far as fjord waters are concerned. The depth-dependent uncertainty displayed for each endmember fraction in Figure S7 is used when computing error bounds on the export of meltwater components from Sermilik (main text, Figure 4).

We note here that the noble gas OMP is more effective in quantifying the concentrations of submarine meltwater than subglacial discharge. This follows from the strong signal in the light noble gases (He, Ne) present in the glacial ice bubbles. Subglacial discharge on the other hand is less well differentiated from other low salinity water masses such as the surface water outside. The uncertainty of the OMP output for subglacial discharge is therefore higher than for submarine meltwater (Fig. S7).

There are two ways to choose the final water mass fraction solution: in one case we could take the solution  $\mathbf{f}$  to the unperturbed system; and in the other we could take

an average of the perturbed solutions  $\bar{\mathbf{f}'}$ . We have chosen to report our OMP solutions in the latter form (this is also the marker displayed in Fig. S7). The solution to the unperturbed system is a single realization of the perturbed systems, no more or less likely than any other solution given the assumptions about uncertainty. The average of the distribution of the perturbed systems is more representative than a single realization. A possible error introduced by this choice arises because the average of the distributions is taken individually over each water mass solution (i.e. AW, PW, SW, SMW, SGD), and therefore the sum of the averages  $\bar{\mathbf{f}'}$  may not be equal to one. In practice, however, the sum of the  $\bar{\mathbf{f}'}$  for all observations is very close to one (r.m.s =  $1 \pm 0.0002$ , Fig. S6).

## 6. Along-fjord Geostrophic Velocity and Glacially Modified Water transport

In order to estimate the export of Glacially Modified Water we calculate the along-fjord geostrophic velocity on the cross-fjord section at  $65.9^\circ\text{N}$  (main text, Fig. 1). We expect that geostrophic balance should hold for the along-fjord flow given that the dominant forcing timescales (3-10 days for synoptic winds, or seasonal for subglacial discharge buoyancy forcing) are much longer than the inertial period, the fjord width is of the order of the Rossby radius (5-8 km), and cross-fjord velocities are small [*Jackson and Straneo, 2016*].

Our cross-fjord section consists of three stations. We use Laplacian interpolation to create a regular, fine, grid for the density field. The density field is extrapolated to the bottom linearly. From the interpolated density field we calculate geostrophic shear and relative geostrophic velocities. We add a barotropic reference velocity to the relative geostrophic velocities so that the resulting depth averaged absolute geostrophic velocity is zero. Zero depth average flow is a reasonable assumption given that the the ‘dead end’

fjord can have no net transport of oceanic waters. However, this assumption neglects the small, a priori unknown, barotropic flux associated with the net freshwater input at the head of the fjord [*Jackson and Straneo, 2016*].

We exclude the upper 10 m of the water column from these calculations. This is because meltwater from the parts of icebergs above the sea surface pools in the very near surface and creates thin layers with very strong horizontal density gradients which are likely not in geostrophic balance.

We know that the fjord velocity field exhibits substantial synoptic variability via shelf-forced baroclinic pumping [*Jackson et al., 2014*]. However, though this variability is the dominant feature in the fall/winter/spring, it is suppressed in the summer [*Jackson et al., 2014; Jackson and Straneo, 2016*]. We cannot guarantee that the synoptic velocity we calculate represents summer-mean estuarine flow we seek to measure. However we expect the estuarine circulation signature to emerge from the diminishing signal of summer-time baroclinic pumping. To check we compare the cross-fjord average of our along-fjord geostrophic velocity against a summer-mean along-fjord velocity profile from a moored ADCP at the same point in the fjord (Fig. S8). The ADCP record is from summer 2013 [*Jackson and Straneo, 2016*], so cannot be directly compared with the time period of our data. However, if we assume that the ADCP record is indicative of the typical summertime circulation, Figure S8 suggests that the observed synoptic circulation during the 2015 cruise was quantitatively similar to the summer-mean.

If order to calculate the flux of submarine meltwater and subglacial discharge we multiply the water mass fraction found from the OMP ( interpolated onto the cross-section grid

of the geostrophic velocity, see main text, Fig. 3 j and k) by the interpolated geostrophic velocity field (main text, Fig. 3i). The total export of SMW and SGD is the area integral of the product of fractions and velocity. The profile show in Figure 4 of the main text is the cross-fjord integrated transport for SMW and SGD at each depth. Uncertainty estimates are found by using the depth-dependent Monte Carlo uncertainty for each water mass OMP solution as depicted in Figure S7.

## References

- Andrews, J. (1985), The isotopic composition of radiogenic helium and its use to study groundwater movement in confined aquifers, *Chemical Geology*, *49*, 339–351.
- Beaird, N., F. Straneo, and W. J. Jenkins (2015), Spreading of Greenland meltwaters in the ocean revealed by noble gases, *Geophysical Research Letters*, *42*, doi: 10.1002/2015GL065003.
- Beaird, N. L., F. Straneo, and W. Jenkins (2017), Characteristics of meltwater export from Jakobshavn Isbræand Ilulissat Icefjord, *Annals of Glaciology*, *74*(10.1017/aog.2017.19).
- Castro, M. (2004), Helium sources in passive margin aquifers – new evidence for a significant mantle  $^3\text{he}$  source in aquifers with unexpectedly low in situ  $^3\text{he}/^4\text{he}$  production, *Earth and Planetary Science Letters*, *222*, 897–913.
- COESA (1976), COESA (1976) U.S. Standard Atmosphere, U.S. Government Printing Office, Washington, D.C.
- Craig, H., and P. Scarsi (1997), Helium isotope stratigraphy in the gisp-2 ice core., *EOS Transactions AGU*, *78*(7).

- Craig, H., Y. Horibe, and T. Sowers (1988), Gravitational separation of gases and isotopes in polar ice caps, *Science*, *242*(4886), 1675–1678.
- Gade, H. G. (1979), Melting of ice in Sea Water: A Primitive Model with Application to the Antarctic Ice Shelf and Icebergs, *Journal of Physical Oceanography*, *9*, 189–198.
- Glover, D., W. Jenkins, and S. Doney (2011), *Modeling Methods for Marine Science*, Cambridge University Press, The Edinburgh Building, Cambridge CB2 8RU, UK.
- Jackson, R. H., and F. Straneo (2016), Heat, Salt, and Freshwater Budgets for a Glacial Fjord in Greenland, *Journal of Physical Oceanography*, *46*(9), 2735–2768, doi:10.1175/JPO-D-15-0134.1.
- Jackson, R. H., F. Straneo, and D. A. Sutherland (2014), Externally forced fluctuations in ocean temperature at Greenland glaciers in non-summer months, *Nature Geoscience*, *7*(7), 503–508, doi:10.1038/ngeo2186.
- Karstensen, J., and M. Tomczak (1998), Age determination of mixed water masses using CFC and oxygen data, *Journal of Geophysical Research: Oceans*, *103*(C9), 18,599–18,609, doi:10.1029/98JC00889.
- Loose, B., and W. J. Jenkins (2014), The five stable noble gases are sensitive unambiguous tracers of glacial meltwater., *Geophysical Research Letters*, *41*, doi:10.1002/2013gl058804.
- Loose, B., P. Schlosser, W. M. Smethie, and S. Jacobs (2009), An optimized estimate of glacial melt from the Ross Ice Shelf using noble gases, stable isotopes, and CFC transient tracers, *Journal of Geophysical Research*, *114*(C8), C08,007, doi:10.1029/2008JC005048.

- Lott, D. (2001), Improvements in noble gas separation methodology: a nude cryogenic trap, *Geochemistry, Geophysics, Geosystems* 2, doi:10.129/2001GC000202.
- Lott, D., and W. Jenkins (1984), An automated cryogenic charcoal trap system for helium isotope mass spectrometry, *Review of Scientific Instruments*, 55, 1982–1988.
- Lott, D., and W. J. Jenkins (2013), A Determination of He, Ne, Ar, Kr, and Xe Solubility Concentrations in Water and Seawater, *Internal Report 1*, Woods Hole Oceanographic Institution, Isotope Geochemistry Facility.
- Lüthi, M. P., C. Ryser, L. C. Andrews, G. A. Catania, M. Funk, R. L. Hawley, M. J. Hoffman, and T. A. Neumann (2015), Heat sources within the Greenland Ice Sheet: dissipation, temperate paleo-firn and cryo-hydrologic warming, *The Cryosphere*, 9(1), 245–253, doi:10.5194/tc-9-245-2015.
- Martinerie, P., D. Raynaud, D. Etheridge, J. Barnola, and D. Mazaudier (1992), Physical and climatic parameters which influence the air content in polar ice, *Earth and Planetary Science Letters*, 112, 1–13.
- Marty, B., B. Upton, and R. Ellam (1998), Helium isotopes in early tertiary basalts, northeast greenland: Evidence for 58ma plume activity in the north atlantic iceland volcanic province, *Geology*, 26, 407–410.
- Morrison, P., and J. Pine (1955), Radiogenic origin of helium isotopes in rock, *Annals of the New York Academy of Sciences*, 62, 69–92.
- Stanley, R., B. Baschek, D. Lott, and W. Jenkins (2009), A new automated method for measuring a new automated method for measuring noble gases and their isotopic ratios in water samples, *Geochemistry Geophysics Geosystems* 10, Q05008, doi:

05010.01029/02009GC002429.

Straneo, F., D. A. Sutherland, D. Holland, C. Gladish, G. S. Hamilton, H. Johnson, E. Rignot, Y. Xu, and M. Koppes (2012), Characteristics of ocean waters reaching Greenland's glaciers, *Annals of Glaciology*, *53*(60), 202–210, doi:10.3189/2012AoG60A059.

Sutherland, D. A., and F. Straneo (2012), Estimating ocean heat transports and submarine melt rates in Sermilik Fjord, Greenland, using lowered acoustic Doppler current profiler (LADCP) velocity profiles, *Annals of Glaciology*, *53*(60), 50–58, doi:10.3189/2012AoG60A050.

Tomczak, M., and D. G. B. Large (1989), Optimum multiparameter analysis of mixing in the thermocline of the eastern Indian Ocean, *Journal of Geophysical Research: Oceans*, *94*(C11), 16,141–16,149, doi:10.1029/JC094iC11p16141.

Torgersen, T., S. Drenkard, M. Stute, P. Schlosser, and A. Shapiro (1995), Mantle helium in ground waters of eastern north america: time and space constraints on sources, *Geology*, *23*, 675–678.

Young, C., and J. Lupton (1983), An ultratight fluid sampling system using cold-welded copper tubing, *EOS Transactions AGU*, *64*, 735.

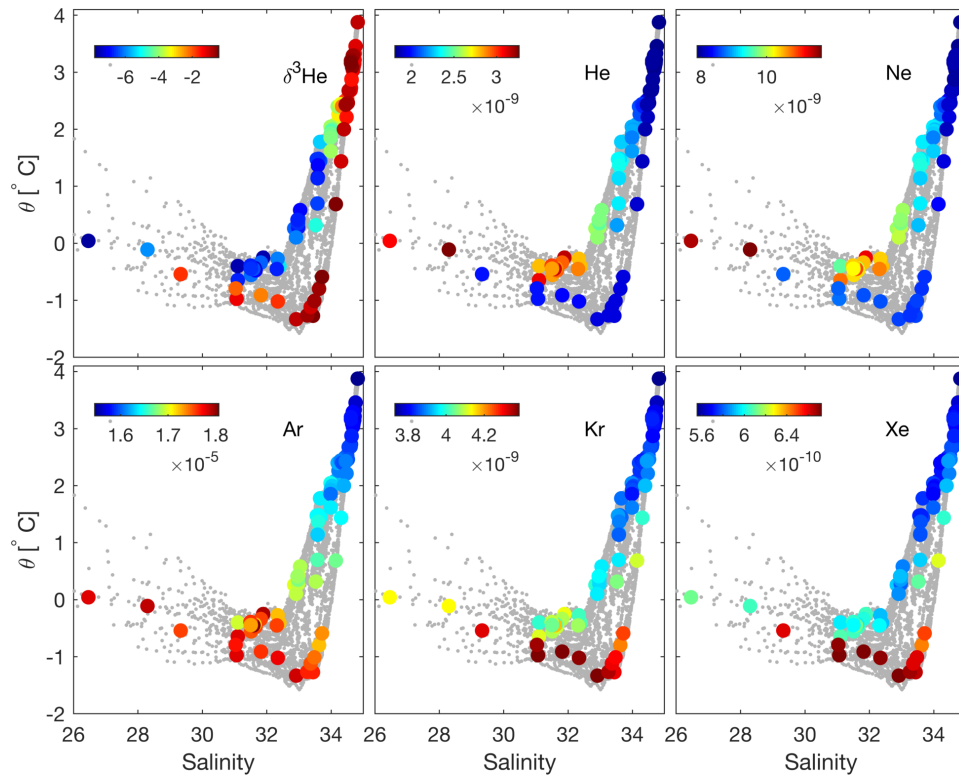


**Figure S1.** Noble gas measurements (color) in  $\theta/S$  space along with all  $\theta/S$  (gray) values in the background. Color indicates noble gas concentrations in mols/kg except the upper left panel of  $\delta^3\text{He}$  which is in percent.

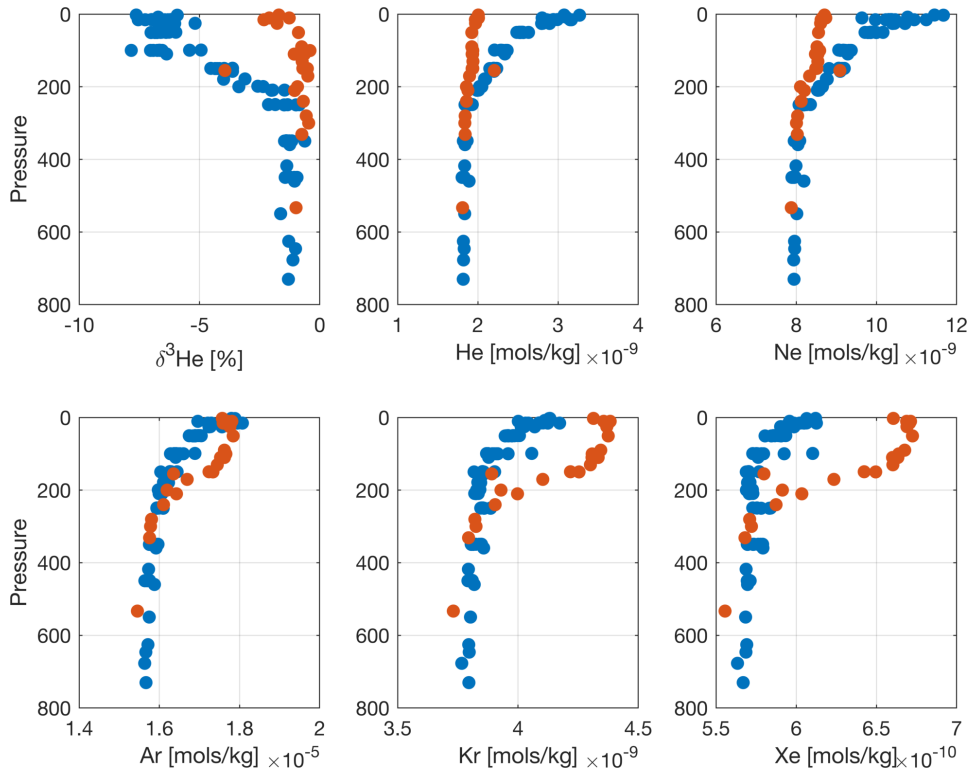


**Figure S2.** Noble gas measurements vs pressure from inside Sermilik Fjord in blue and outside the fjord in orange.

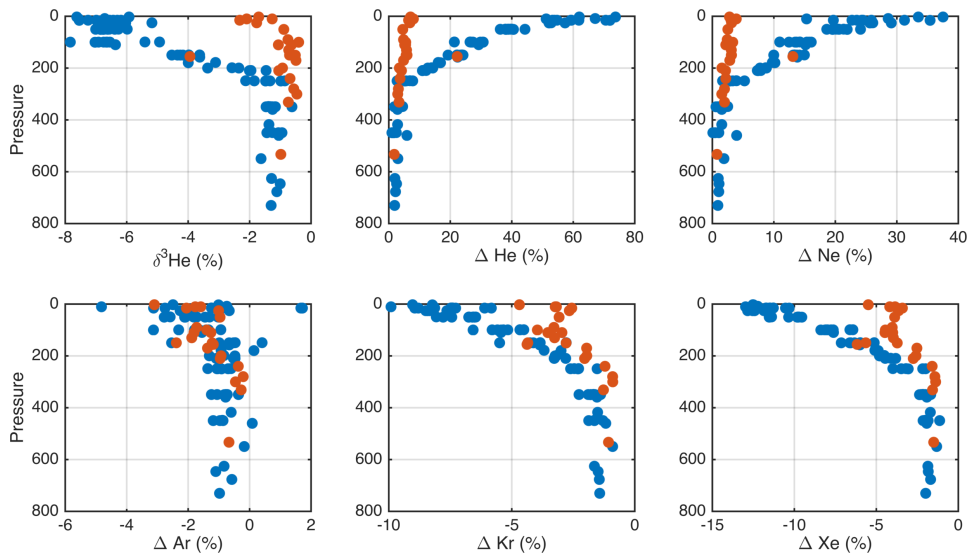


**Figure S3.** Noble gas measurements as saturation anomalies vs pressure from inside Sermilik Fjord in blue and outside the fjord in orange.

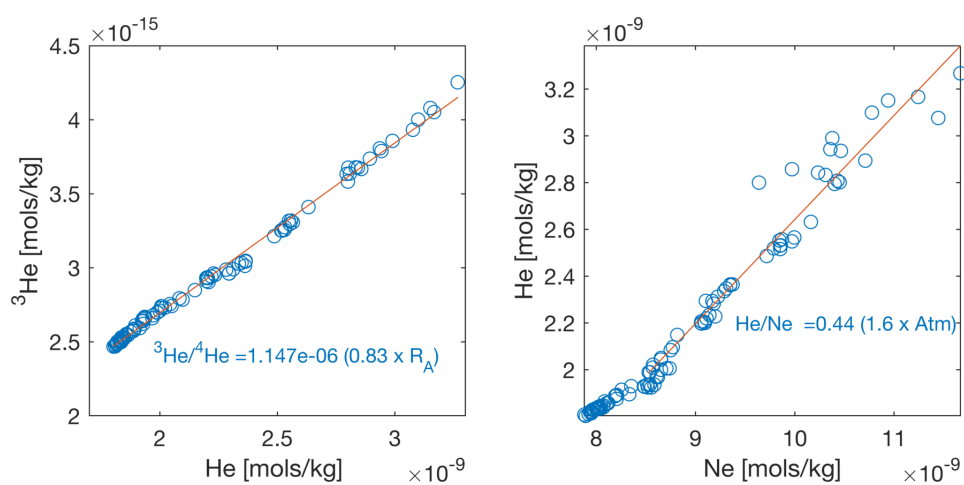


**Figure S4.**  $^3\text{He}/\text{He}$  (left) and  $\text{He}/\text{Ne}$  (right) ratios for water samples taken in Sermilik.

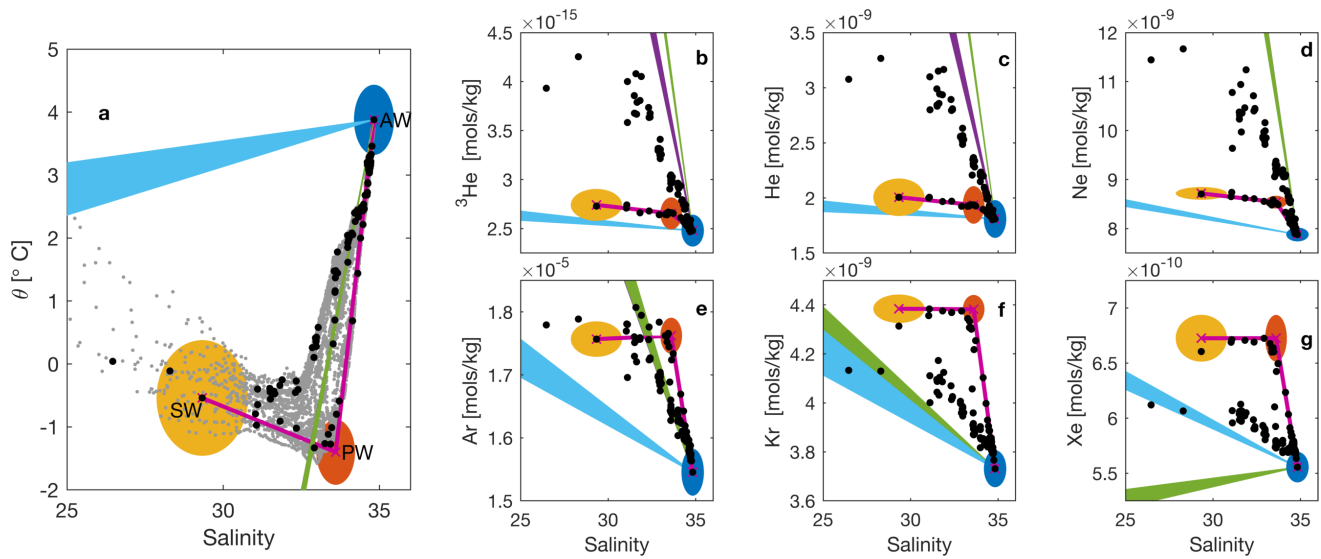


**Figure S5.** Water mass definitions for Sermilik data. Temperature (**a**) and each noble gas measurement (**b-g**:  $^3\text{He}$ , He, Ne, Ar, Kr, Xe) plotted against salinity (black dots). In each panel the colored ellipse shows the range of perturbed endmember values for AW (blue), PW (orange), and SW (yellow) for each of the perturbed systems, **A**, in the Monte Carlo simulation (Section 5.3). Colored line patches show the range of mixing lines between AW and the perturbed endmember values for SGD (light blue), AIM (purple), and SMW (green), bounded by the maximum and minimum perturbed values. The magenta line connects the three ambient ocean water masses. In panel **a**, all temperature-salinity data is shown in gray.

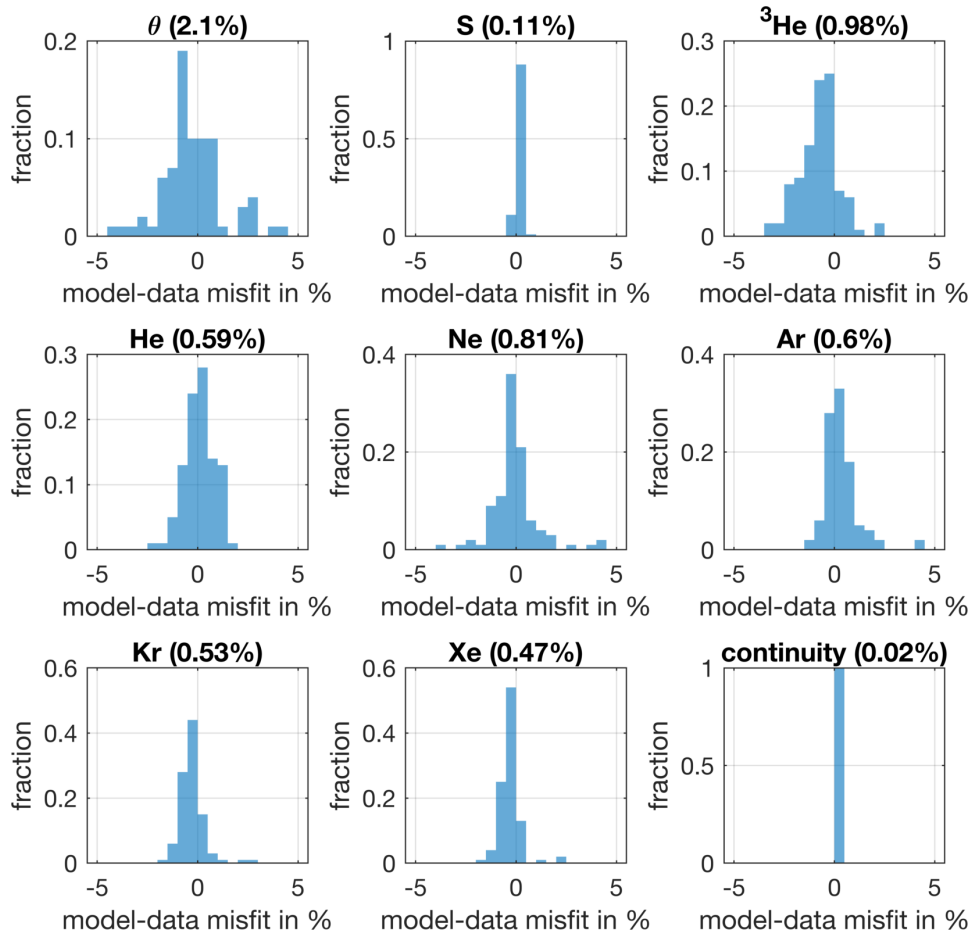


**Figure S6.** Distribution of model-data misfit of the OMP for each parameter. The root-mean-square misfit as a percentage is printed for each parameter in parenthesis next to the label.

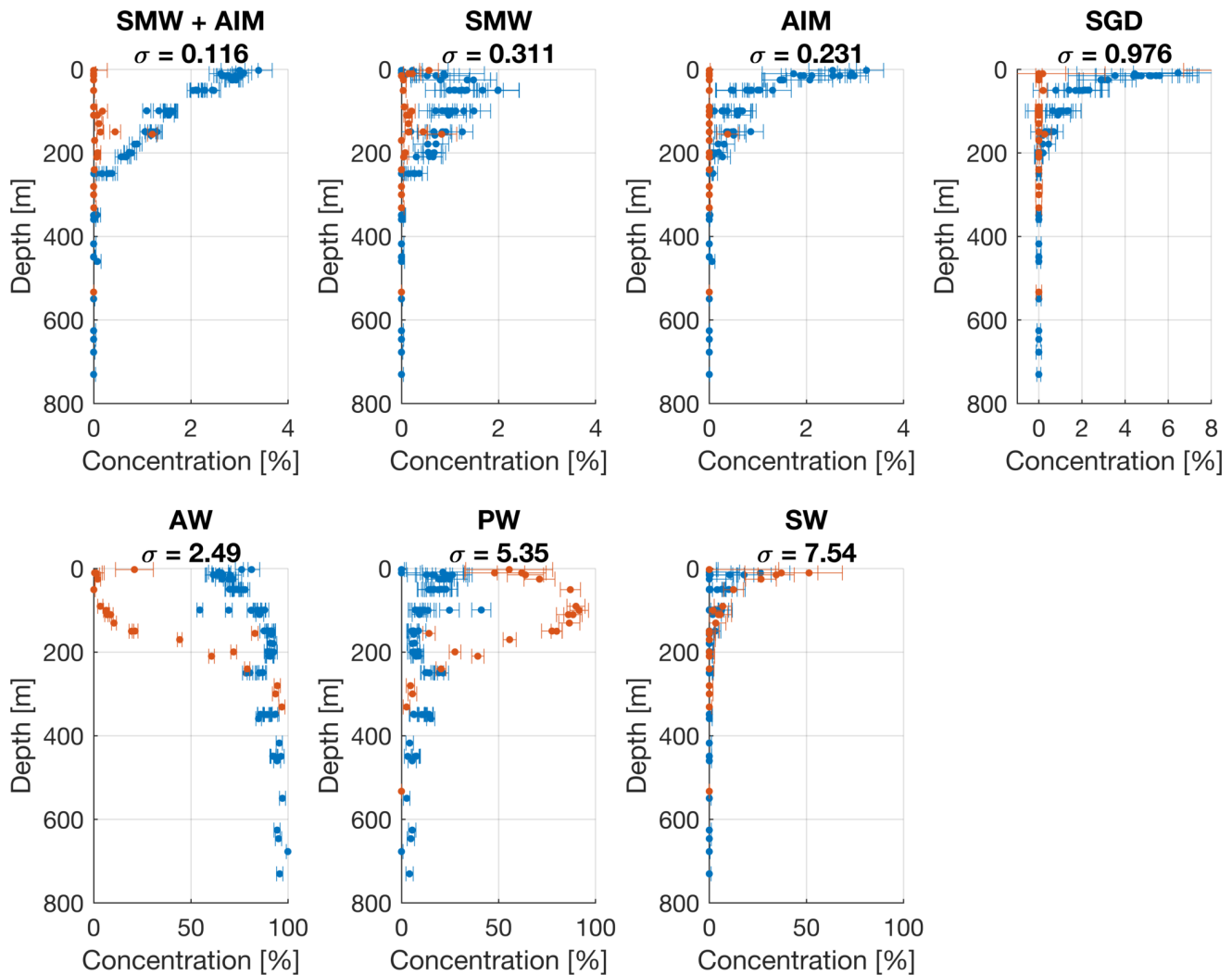


**Figure S7.** Depth profiles of the OMP fraction solutions for each sample. Orange markers are from stations outside the fjord, blue markers inside the fjord. Each solution is bounded by a horizontal errorbar showing  $\pm$  one standard deviation of the perturbed solutions for that observation. Mean standard deviations are printed in the title of each panel. The top left panel shows the sum of the submarine meltwater and ancient ice melt endemblers – the field that is used as submarine meltwater in the main text.

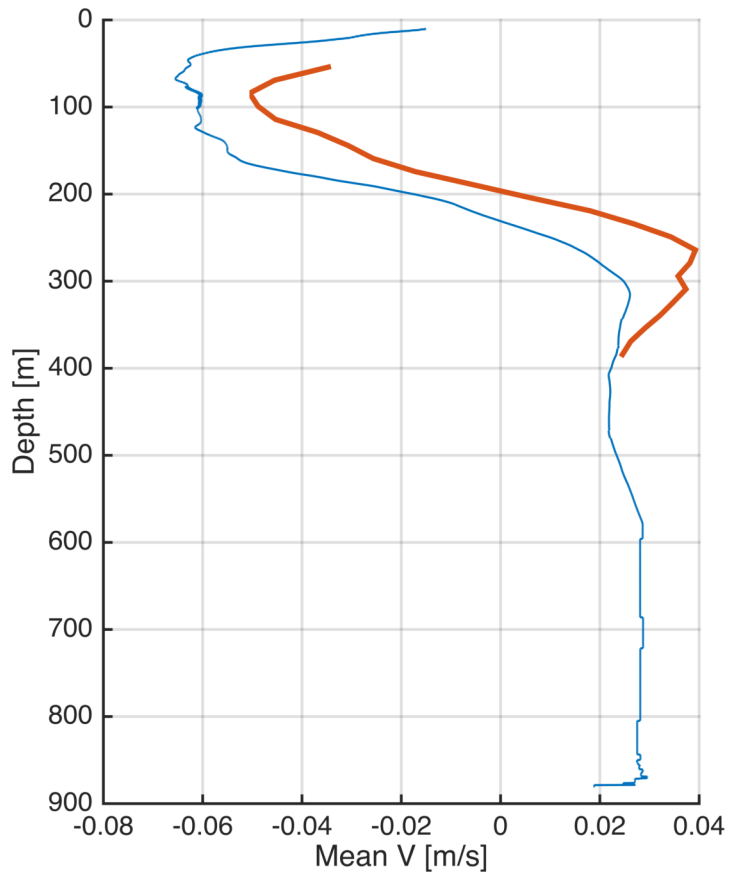


**Figure S8.** Depth profile of 2013 summer-long mean ADCP measured velocity from mid-fjord mooring (orange, *Jackson and Straneo* [2016]) and the cross-fjord average of the along-fjord geostrophic velocity (blue) computed from the section presented in the text. Positive velocities are towards the glacier, negative velocities are towards the shelf.

**Table S1.** Endmember Parameter values. All gases in units mols/kg, multiplicative order of magnitude indicated in the first row. Potential temperature in units °C, salinity in PSU.  $\epsilon_j^{max}$  is the maximum uncertainty of all endmember values for each parameter. Errors listed are the analytical error as a percent.

Water Mass	$\theta$ °C	Salinity	$^3\text{He}$ [ $10^{-15}$ ]	He [ $10^{-9}$ ]	Ne [ $10^{-9}$ ]	Ar [ $10^{-5}$ ]	Kr [ $10^{-9}$ ]	Xe [ $10^{-10}$ ]
AW	3.46	34.76	2.479	1.809	7.879	1.545	3.731	5.556
PW	-1.40	33.60	2.654	1.937	8.540	1.762	4.382	6.726
SW	-0.54	29.33	2.742	2.006	8.718	1.757	4.384	6.726
SGD	0	0	3.001	2.209	10.07	2.176	5.432	8.412
SMW	-87	0	36.24	26.19	88.73	4.546	5.779	4.536
AIM	-87	0	47.34	41.27	88.73	4.546	5.779	4.536
$\epsilon_j^{max}$	4	2	2.69	2.095	7.099	0.364	0.462	0.684
Error %	0.2	0.2	0.15	0.18	0.18	0.13	0.19	0.14
Weights	96	81	27	27	25	11	3	4

**Table S2.** Uncertainty estimates ( $\epsilon_{ij}$ ) used to perturb the design matrix in the Monte Carlo simulation. All gases in units mols/kg, multiplicative order of magnitude indicated in the first row. Potential temperature in units °C, salinity in PSU.

Water Mass	$\theta$ °C	Salinity	$^3\text{He}$ [ $10^{-15}$ ]	He [ $10^{-9}$ ]	Ne [ $10^{-9}$ ]	Ar [ $10^{-5}$ ]	Kr [ $10^{-9}$ ]	Xe [ $10^{-10}$ ]
AW	0.1	0.1	0.012	0.009	0.04	0.008	0.02	0.04
PW	0.1	0.1	0.009	0.007	0.03	0.006	0.01	0.02
SW	1	2.0	0.01	0.008	0.03	0.007	0.02	0.03
SGD	2	0.01	0.04	0.03	0.245	0.12	0.37	0.684
SMW	4	0.01	2.69	2.095	7.099	0.36	0.46	0.362
AIM	4	0.01	2.69	2.095	7.099	0.36	0.46	0.362